A paintbrush for delivery of nanoparticles and small molecules to live cells with micrometer spatial and millisecond temporal control

Cornelia Holler*[1,2], Richard W. Taylor*[1,2], Alexandra Schambony[1,2,3], Leonhard Möckl[1,2], and Vahid Sandoghdar†[1,2,4]

[1]Max-Planck-Zentrum für Physik und Medizin, Erlangen, 91058, Germany.
[2]Max Planck Institute for the Science of Light, Erlangen, 91058, Germany.
[3]Developmental Biology, Friedrich-Alexander University Erlangen-Nürnberg, Erlangen, 91058, Germany.
[4]Department of Physics, Friedrich-Alexander University Erlangen-Nürnberg, Erlangen, 91058, Germany.
*Contributed equally
†To whom correspondence should be addressed. E-mail: vahid.sandoghdar@mpl.mpg.de

Contents

1 Pipette Fabrication, Geometry & Performance

1.1 Micropipette Fabrication

Borosilicate glass capillaries with an outer diameter $\varnothing_{\text{out}} = 1\,\text{mm}$ and inner diameter $\varnothing_{\text{in}} = 0.78\,\text{mm}$ (GB100TF-10, Science Products GmbH) were cleaned in a series of 10 min sonication steps, first in 2% Hellmanex, followed by double-distilled water and ethanol. Capillaries were then dried using a heating plate and plasma-cleaned afterwards. Before pulling, capillaries are incubated in 37% HCl overnight, rinsed with double-distilled water and dried, then plasma-cleaned prior to pulling. A Sutter P-2000 Micropipette Fiber Puller is used to draw the capillaries into the desired micropipettes using the program given in Table 1. The program is completed in three lines.

Heat	Filament	Velocity	Delay	Pull
400	5	200	255	0

Table 1: Pull settings to draw micropipette with high-aspect ratio taper and tip-$\varnothing_{\text{in}} = 1\,\mu$m using a P-2000 Sutter Fiber Puller.

The drawn micropipettes are shown in Fig. 1a-c and feature a high-aspect ratio taper, denoted L (Fig. 1a) and $\varnothing_{\text{in}} = 1\,\mu$m at the tip (Fig. 1b,c). The capillaries feature an in-built filament (marked with arrowhead in Fig. 1c) which aids with back-filling of the pipette through capillary forces.

To accommodate the micropipette on a microscope where the imaging objective occupies the sample space, the tapered length of the micropipette is angled with respect to the main shaft. To introduce this angle, the taper undergoes additional working with a focused CO_2 laser, shown in Fig. 1d. The pulled pipette is securely mounted within a grip head (Eppendorf) and positioned within the focus of the laser using a micropositioner such that the focus is a length L away from the tip. The laser is operated in pulsed mode, which instantly softens the glass in the focal volume, causing the taper to self-bend towards the laser source, shown in Fig. 1d,e. A stop rod in the path of the bending tip fixes the desired angle θ angle to which the tip will bend. With no stop, the tip can bend to a full $\theta_{\text{max}} = 90°$.

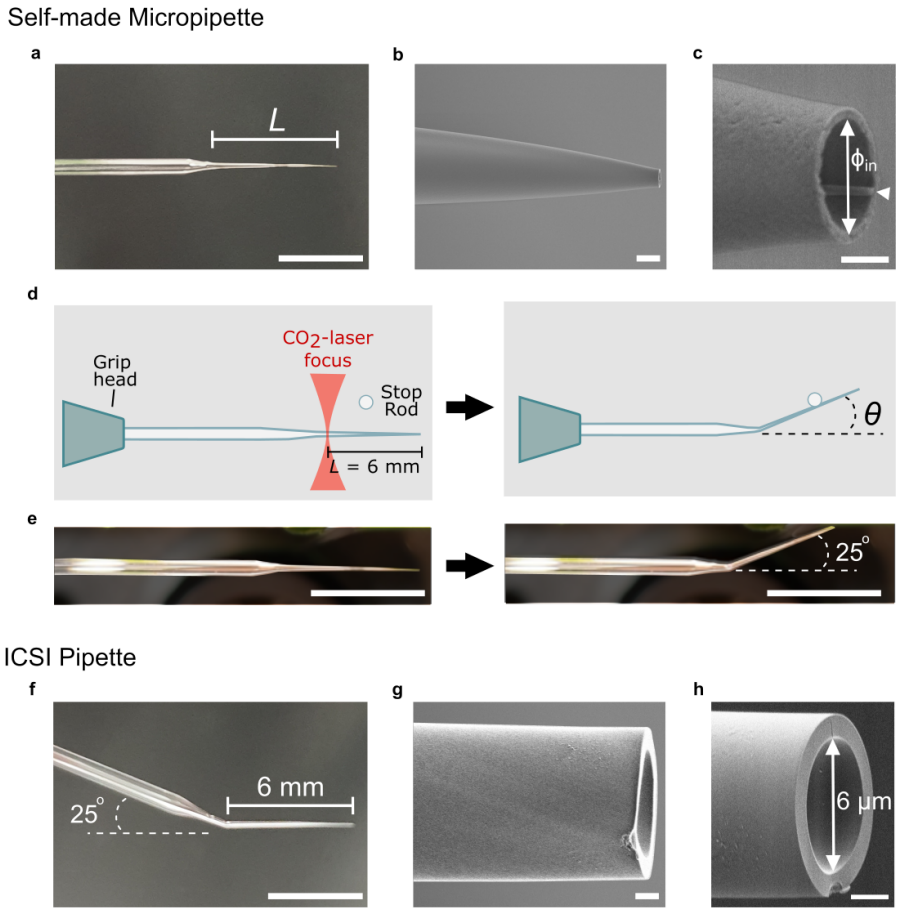

Figure 1: Micropipette fabrication and geometrical form. a, Photograph showing a pulled micropipette with a long, thin taper of length $L = 6\,\text{mm}$. Scale bar 5 mm. **b** and **c**, SEM images of the pipette shown in (**a**), visualizing the very end of the tip taper (**b**) and the micron-sized aperture (of diameter $\varnothing_{\text{in}} = 1\,\mu\text{m}$) with built-in filament (**c**). Scale bars in (**b**) and (**c**) $1\,\mu\text{m}$ and 500 nm, respectively. **d,** Schematic visualization of the process to introduce an angle to the taper. The pulled micropipette is mounted into a grip head and positioned into the focus of a CO_2-laser, with the focus a distance $L = 6\,\text{mm}$ from the tip. Upon heating, the taper bends towards the laser source and a stop rod fixes the angle to θ. **e**, Photographs showing a pulled micropipette before and after the angle-forming process, here with $\theta = 25^\circ$. Scale bar 5 mm. **f,** Photograph showing an Eppendorf ICSI micropipette with $L = 6\,\text{mm}$ and $\theta = 25^\circ$. Scale bar 5 mm. **g, h,** SEM images of the pipette shown in (**f**), highlighting the linear taper towards the very tip (**g**) and the aperture detail (**h**), wherein $\varnothing_{\text{in}} = 6\,\mu\text{m}$. Scale bars in (**g**) and (**h**) $1\,\mu\text{m}$ and $2\,\mu\text{m}$, respectively.

For micropipettes with similar forms, but larger apertures ($\varnothing_{\mathrm{in}}$), commercially available pipettes from Eppendorf are used (Piezo Drill Tip M.ICSI pipettes, referred to here as ICSI for short). These micropipettes are characterized by inner diameters of $\varnothing_{\mathrm{in}} = 6\,\mu$m, $L = 6\,$mm and $\theta = 25°$, shown in Fig. 1f-h. Owing to the larger inner diameter of the micropipettes, a filament is not required and the pipettes can be filled using a microloader pipette.

1.2 Micropipette Hydrodynamic Resistance

When fully-developed laminar flow is confined to a channel, one can approximate that rate of fluid flow (Q) is linearly proportional to the pressure drop across the channel (Δp): a scenario which applies to our micropipettes. The constant of proportionality is the hydrodynamic resistance ($\mathrm{R_H}$):

$$\mathrm{R_H} = \frac{\Delta \mathrm{p}}{\mathrm{Q}} \tag{1}$$

The hydrodynamic resistance R_{H} is a function of the geometry of the channel, as well as the viscosity of the fluid in the channel and the nature of the slip-condition between the fluid and channel wall, and serves as a useful characterization of the micropipette performance. This is most evident with the reciprocal of hydrodynamic resistance, known as hydrodynamic conductance C_{H}, which reports on the resultant fluid flow rate within the pipette as a function of applied air pressure.

We measure the hydrodynamic resistance of our ICSI pipettes in both injecting and aspirating operation. We do so on the same pipette to avoid inter-pipette variation in the characterization. All pressures refer to that which is applied by the pressure regulator (Elveflow OB3+). To determine the fluid flow rate in or out of the micropipette, which is in the $\mathrm{nL\,s^{-1}}$ range, we firstly fill the micropipette with a fluorescein solution to aid visibility ($1\,\mu\mathrm{g}\,\mu\mathrm{L^{-1}}$ fluorescein solution from sodium salt, Merck, 518-47-8). We apply a constant pressure and image the position of the moving solution meniscus over time. With knowledge of the internal geometry of the channel, the shift in meniscus position can be computed as a change in the internal solution volume, which we average over time assuming steady-state operation. Repeating for a range of applied pressures, one can calculate the corresponding induced flow rate - shown in Fig. 2.

1.3 Positioning the Apertures of the Micropipettes

As illustrated in Fig. 3, the μkiss device consists of two similar micropipettes placed adjacent to one another, such that fluid flow out of one tip is subsumed within the inward flow of the second. This is accomplished by positioning the two tips side-by-side so that their apertures lie in the same plane (Fig. 3). The tapers of the two micropipettes lie at an angle of $\theta_{xy} = 35°$ in the mutual plane of their alignment. There is no other relative angle between the two tips in other planes ($\theta_{yz} = \theta_{xz} = 0°$). Small offsets between the contacting outer walls of the tips in the xy plane, denoted $x_{\mathrm{separation}}$ and $y_{\mathrm{separation}}$ in Fig. 3 are introduced to aid flow confinement and adjust brush shape. Typically $x_{\mathrm{separation}} = 1\,\mu$m and $y_{\mathrm{separation}} = 0 - 2\,\mu$m. No offset is introduced in the z-direction, $z_{\mathrm{separation}} = 0\,\mu$m.

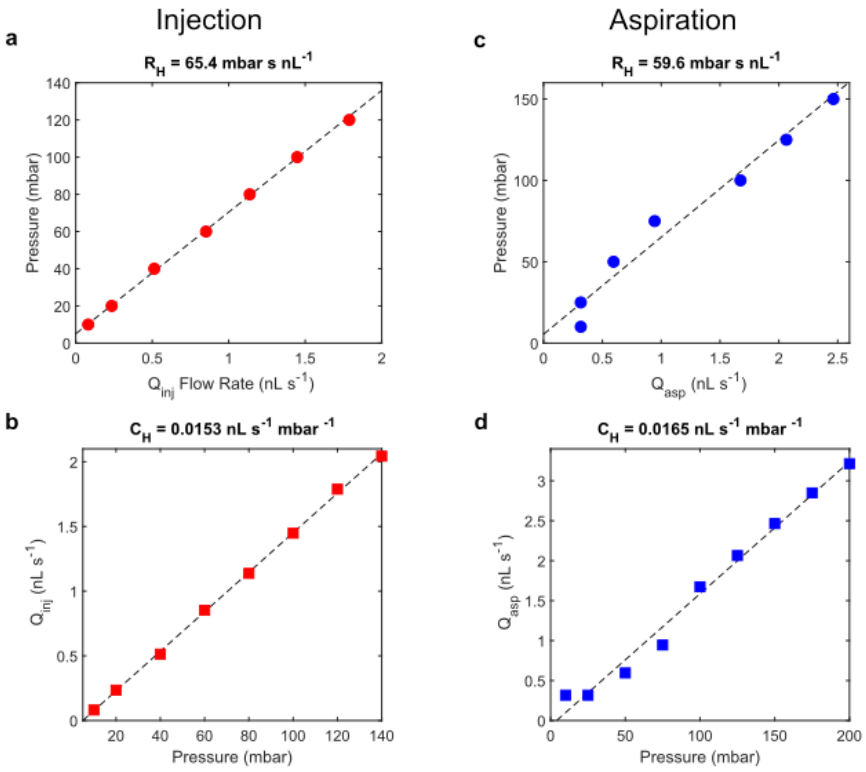

Figure 2: Hydrodynamic resistance and conductance of an ICSI pipette under both aspiration and injection operation. **a** and **b**, under application of positive pressure (injection operation) the hydrodynamic resistance (**a**) and conductance (**b**). **c** and **d**, Under application of negative pressure (aspiration operation) the hydrodynamic resistance (**c**) and conductance (**d**).

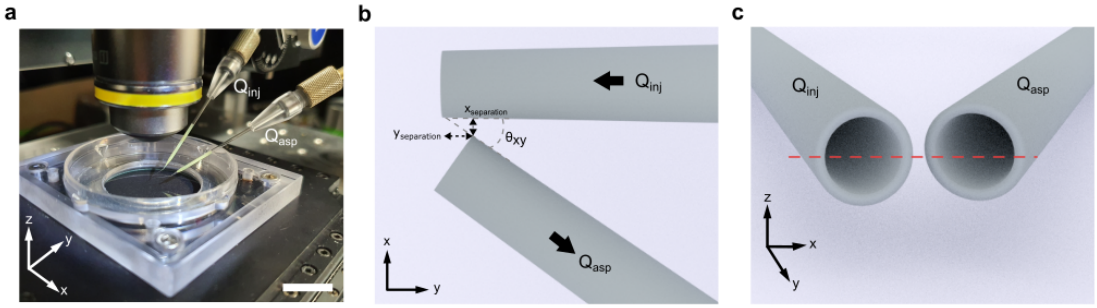

Figure 3: Orientating two micropipettes for μkiss brushing. a, Photograph showing two micropipettes forming the μkiss device *in-situ* within a cell-bearing dish and with an imaging objective above. Scale bar 1 cm. **b,** Illustration of the spatial arrangement of the two micropipette tips, as viewed top-down (x-y plane). **c,** Alternate perspective from (**b**), showing the apertures are aligned, with no out-of-plane offset or rotation.

Description	Parameter	Value	Unit
Flow rate injected	Q_{inj}	0-2	$\mathrm{nL\,s^{-1}}$
Flow rate aspirated	Q_{asp}	0-2	$\mathrm{nL\,s^{-1}}$
inner diameter	$\varnothing_{in}$	6	μm
wall thickness	wall_thick	1	μm
separation in x	x_separation	0	μm
separation in y	y_separation	1	μm
separation in z	y_separation	1	μm
angle in x-y	θ_{xy}	35	degree
angle in y-z	θ_{yz}	0	degree
angle in x-z	θ_{xz}	0	degree

Table 2: Parameters and their values used for modeling the μkiss envelope in COMSOL.

1.4 Positioning the μkiss Apertures on the Sample

Positioning the μkiss apertures vertically involves placing the tip-pair at a height above the target surface such that, upon the establishment of the flow envelope, reagent transfer occurs between envelope and surface. This is readily achieved when imaging with a water-dipping objective by one of two methods. One approach is to first bring the target surface into focus, then raising the objective up a distance slightly larger than the aperture diameter of the μkiss apertures tips. The μkiss apertures, initially situated far away from the target surface, is lowered towards the surface until the full-width of the aperture is in sharp focus. The apertures should now lie close to the target surface without having made contact. The focus can be returned to the plane of the target surface and labeling can begin.

A second approach is to begin with the μkiss apertures running, with envelope established, at a height far above the target surface. With the imaging plane set to the target surface, the μkiss apertures can be lowered progressively until the lower side of the envelope begins to enter the focal depth of the objective (here, the depth of focus is ca. $0.75\,\mu$m) and then lowered further until the desired intersection between envelope and surface (that is, brush-stroke area) is achieved.

1.5 COMSOL Modeling

COMSOL Multiphysics 6.0 (COMSOL, AG) is used to numerically solve the Navier-Stokes equation for single-phase laminar flow for the dual pipette geometry. The modeled geometry is shown in Fig. 4 and is modeled with an extra fine Physics-controlled mesh (generated by COMSOL) for both stationary and time-dependant solutions. The single phase flow module (spf module) is used, with physical and geometric parameters given in Table 2. Modeling is performed in full in three dimensions as well as in two dimensions for the xy-plane subtending the centers of both pipettes, illustrated in red in Fig. 4c for clarity.

The micropipette apertures are modeled within an encompassing cubic domain filled with water, representing the open fluidic bath environments. A boundary condition at the cube walls assumes the net pressure remains static at environmental pressure and permits flow in and out of the domain. Borosilicate glass is the material assumed for all micropipette glass surfaces and a no-slip conditions asserted at glass-water boundaries. Boundary conditions

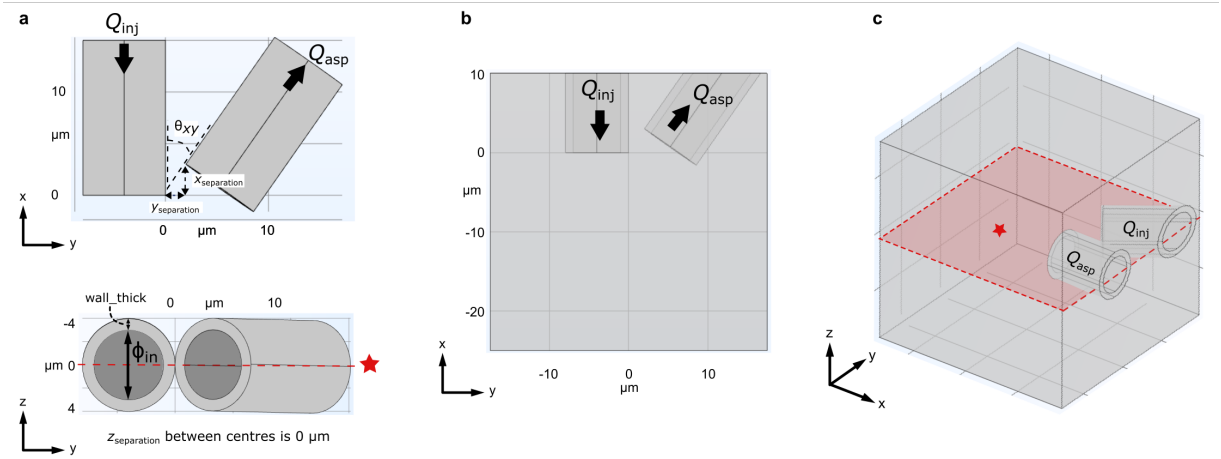

Figure 4: Schematics showing the COMSOL modeling geometry for the μkiss apertures. **a,** xy- and zy-projections of the two tip sections with geometrical parameters marked. Red dashed line marks a plane subtending the two centres of the tips in the xy-plane. **b,** xy-projection of the tips with encompassing 'open-environment' cubic domain shown. **c,** The complete domain shown in (**b**), shown in full three-dimensional projection and with the mid-plane introduced in (**a**) marked for clarity.

for micropipette walls assert the glass is non-permeable to water. To visualize transport of dissolved species, the transport of dilute species module (tds module) is used, with transport via convention enabled. The velocity field used to compute transport is that solved in the previous step by the spf module for the same geometry. Boundary conditions assume the aperture where Q_{inj} enters is the only source of the dilute species and that the aperture where Q_{asp} is defined also acts as a sink of the dilute species in addition to all the walls of the encompassing cubic domain. No flux of the dilute species occurs through the glass walls, and the initial concentration of dilute species is null.

2 μkiss Envelope Velocimetry

To determine the velocity of fluid flow within the brush envelope, gold nanoparticles are used as tracer particles and high-speed tracking of their positions is performed as they transit through the flowing envelope.

Gold nanoparticles with diameter 80 nm (Solutions EM.GC80/7) were used at a concentration of 1.5×10^{9} particles ml^{-1} (diluted 1:5 in Milli-Q water). A $1\,\mathrm{mg\,ml}^{-1}$ stock solution of fluorescein was prepared (sodium salt, Merck, 518-47-8) and was added in a 1:100 dilution for visualizing the flow envelope through fluorescence. The brush envelope established for the particle velicometry measurement is shown in Fig. 5(a) for $Q_{\mathrm{inj}} = 0.11\,\mathrm{nL\,s}^{-1}$ and $Q_{\mathrm{ratio}} = 0.27$.

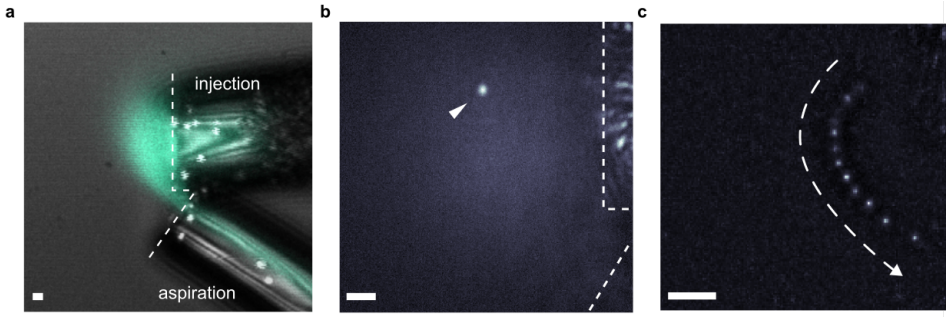

Figure 5: Velocimetry of Flow Envelope through tracking of nanoparticle tracers a, dual confocal iSCAT (gray scale) and confocal fluorescence (green) image showing the positioning of the μkiss apertures and the resulting fluorescently-labeled flow envelope. Dashed lines guide the eye to the pipette apertures. Scale bar is 1 μm. **b**, Raw widefield iSCAT image from the the field of view of **a** with a single nanoparticle particle mid-transit. Dashed lines guide the eye to the pipette apertures, as shown in **a**. Scale bar is 1 μm. **c**, Composite RVT image from a particle tracked across consecutive frames in time. The dashed line guides the eye to the transit path of the particle. Scale bar is 1 μm.

Figure 5b shows a single widefield iSCAT imaging frame wherein a single gold nanoparticle is mid-transit. Widefield iSCAT imaging and particle tracking is performed according to Taylor *et al.*[1]. In this work, the exposure time is 10 μs and the frame rate 10,000 fps. Each imaging frame containing a nanoparticle that is to be tracked is firstly processed by removal of static background features through subtraction of the temporal-median background. Each frame is then converted using the Radial Variance Transform (RVT), with filter radii corresponding to 3, 5 and 7 pixels, to remove ring-features of the point-spread function (PSF)[2]. Figure 5c presents a composite image of the RVT-transformed PSF for consecutive frames for a single gold nanoparticle that is tracked. To each transformed PSF, such as those in Fig. 5c, a two-dimensional Gaussian function is fitted to determine the particle center. By

computing the displacement of the particle between pairs of frames, the instantaneous pair-wise flow velocity is calculated.

3 Characterization of Flow Envelope

3.1 Parameterizing Envelope Extent

To characterize the physical size of the flow envelope, we introduce the extent parameter, L_e, which represents the length by which the envelope protrudes out of the injection pipette and into the open fluidic medium, shown in Fig. 6.

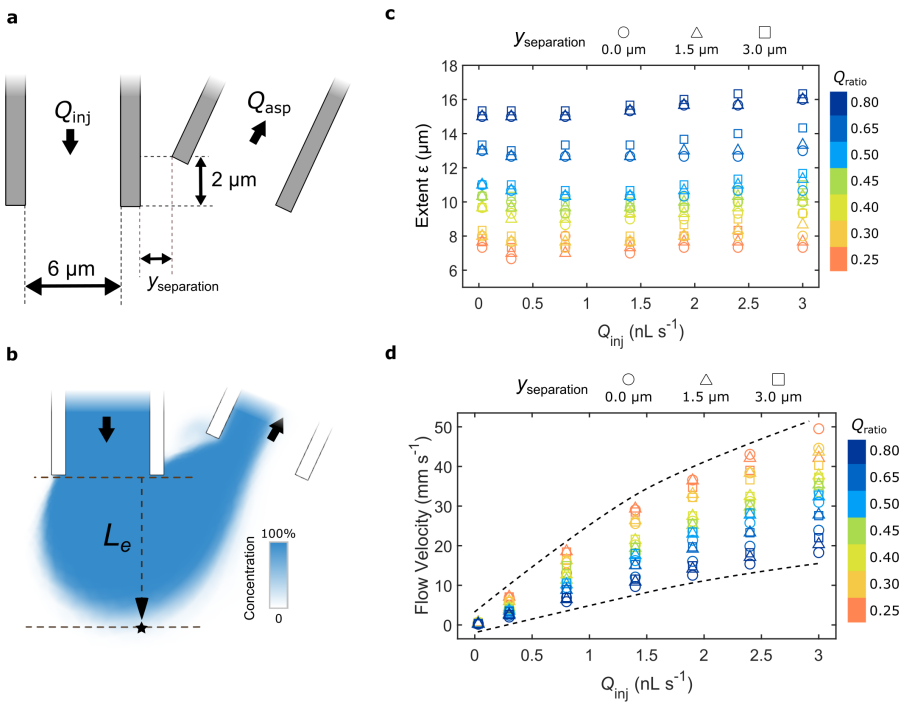

Figure 6: Numerical modeling of the μkiss envelope extent and associated flow velocity. a, Schematic of μkiss apertures geometry used for numerical modeling. Arrows mark the direction of fluid flow. **b,** Computed distribution of reagent material within the flow envelope system for $y_{\text{separation}} = 1.5\,\mu$m. The size parameter - 'extent', L_e, is highlighted. A star-marker guides the eye to the point on the envelope boundary where L_e terminates. **c,** Computed extents for flow envelopes as a function of Q_{inj}, Q_{ratio} and pipette separations. **d,** Computed flow velocities at extent apex (star marker) as a function of the full parameter set for Q_{inj}, Q_{ratio} and pipette separations.

We numerically model the μkiss envelope using the arrangement shown in Fig. 6a,b, for a range of Q_{inj}, Q_{asp} and also $y_{\text{separation}}$. For clarity, we express Q_{asp} through its value relative to Q_{inj}, that is: $Q_{\text{ratio}} = Q_{\text{inj}}/Q_{\text{asp}}$. The

results of numerical modeling is summarized in Fig. 6c. One sees the extent of the envelope is a balance between the injection flow rate Q_{inj} and aspiration flow rate Q_{asp}; independent of micropipette positions, a higher Q_{inj}, relative to Q_{asp}, promotes a larger L_{e}. Alternatively, one may interpret Fig. 6c to indicate that larger Q_{asp} act to curtail L_{e} for all scenario to render a smaller and compact envelope.

It is also instructive to inspect the flow velocity v of the envelope at the boundary point defined by L_{e} (marked by a star in Fig. 6b). In Fig. 6d, the flow velocity at L_{e}, denoted v_{e} is presented.

3.2 Reynolds Number of the Envelope Boundary

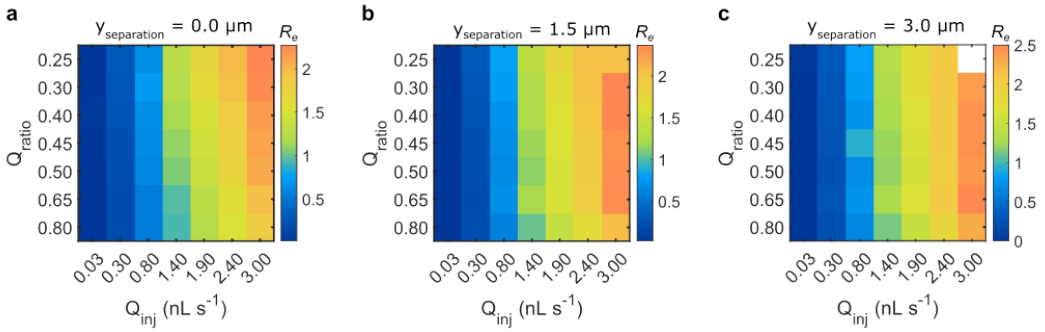

Figure 7: Reynolds numbers computed for the μkiss envelope. Mean Reynolds numbers R_e along the flow envelope boundary for various Q_{inj} and Q_{ratio} for $y_{\mathrm{separation}} = 0.0\,\mu$m **a**, $1.5\,\mu$m **b** and $3.0\,\mu$m **c**.

The Reynolds number provides an indication whether a fluid flow in a particular context is laminar and regular, or turbulent, and can be expressed via:

$$R_{\mathrm{e}} = \frac{\rho v L_{\mathrm{R}}}{\mu} \tag{2}$$

where μ stands for viscosity and ρ signifies the density, in this case of water with values of 1.0016 mPa s and 997 Kg m^{-3}, respectively. The parameter L_{R} denotes the path along which flow occurs, and we may approximate $L_{\mathrm{R}} = \pi\, L_{\mathrm{e}}$ and take the flow velocity v as the flow velocity at maximum extent (L_{e}). The result of the calculation for R_{e} for various Q_{inj}, Q_{ratio} and $y_{\mathrm{separation}}$ is presented in Fig. 7. Across our system, $R_{\mathrm{e}} = 0.006 - 2.5$ and therefore the assumption of laminar flow is supported.

3.3 Péclet Number at Envelope Boundary

The Péclet number is a measure of the convective versus diffusive transport, and helps one evaluate whether one can achieve strong confinement of a dilute species - that is, a sharp boundary between the reagents of the confined envelope and the open fluidic environment, which should otherwise be free of the reagents. In a pragmatic sense, the Péclet number identifies if the flow velocity is 'too slow', and is permitting sufficient time for the reagents to diffuse out of the regular directed path of the laminar flow jet. Such an effect manifests as a broadening of the

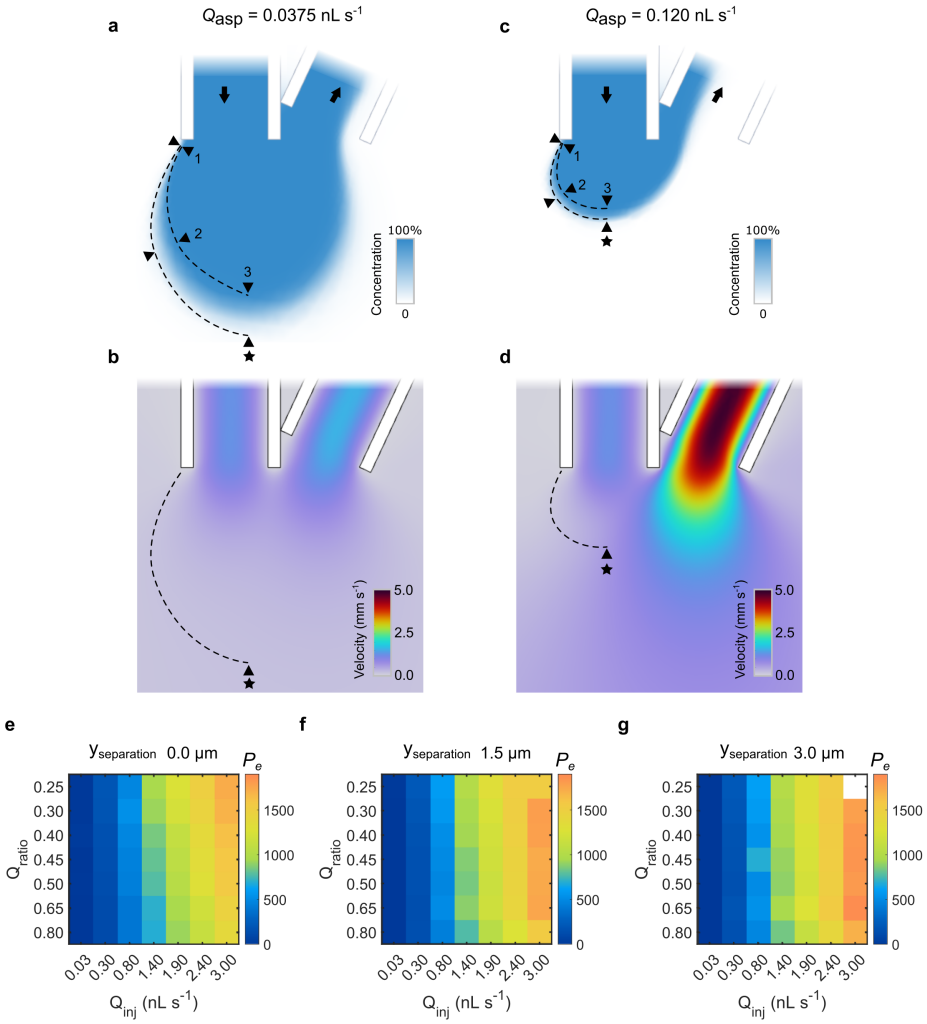

Figure 8: Diffusion-led broadening of the flow envelope and Péclet number. a, Simulated steady-state distribution of reagent (blue) within a flow envelope with $Q_{\mathrm{inj}} = 0.03\,\mathrm{nL\,s^{-1}}$ and $Q_{\mathrm{asp}} = 0.0375\,\mathrm{nL\,s^{-1}}$ **a, b**, and the corresponding flow velocity field $\mathbf{v}$ (**b**). Star marker guides eye to corresponding feature points. **c**, a contrasting scenario to (**a**), with here a larger $Q_{\mathrm{asp}} = 0.12\,\mathrm{nL\,s^{-1}}$. and $Q_{\mathrm{inj}} = 0.03\,\mathrm{nL\,s^{-1}}$. **d,** The corresponding flow velocity field from (**c**). Star marker guides eye to corresponding feature points. **e**, Péclet number P_e along the flow envelope boundary for various Q_{inj} and Q_{ratio} for **e**, $y_{\mathrm{separation}} = 0.0\,\mu$m, **f**, $1.5\,\mu$m and **g** $3.0\,\mu$m .

envelope boundary, depicted in Fig. 8 for two such cases where the injection rate is the same ($Q_{\mathrm{inj}} = 0.03\,\mathrm{nL\,s^{-1}}$) but the Q_{asp} varies. In Fig. 8a,b - where $Q_{\mathrm{ratio}} = 0.80$, diffusion-led broadening is larger. Inspecting the numbered markers as one progresses around the envelope reveals a widening of the envelope boundary (Fig. 8a), which is a result of the low flow velocities in this region (Fig. 8b). We define the edge of the boundary to be the point at which the concentration of the envelope falls to 1%. The star marker acts as a guide to the eye. By increasing Q_{asp}, shown in Fig. 8c,d, the envelope boundary remains crisp (Fig. 8c) as the flow velocity in this region is now larger

(Fig. 8d). In both cases, shown in Fig. 8, the reagents remain confined to the envelope, only their distribution at the envelope is affected. In addition, past the point of maximum extent, the boundary becomes more confined owing to the higher flow velocities associated with the aspiration micropipette. For this reason, the envelope at the point of ϵ - shown by the star marker in Fig. 8, is the point where broadening is often largest.

The Péclet number (P_{e}) parameterizes the strength of diffusion-led broadening of convective flow, and is given by:

$$P_{\mathrm{e}} = \frac{vL_{\mathrm{R}}}{D} \tag{3}$$

where D is the diffusion constant of the reagent, here $D = 1.34\,\mu\mathrm{m}^2\mathrm{s}^{-1}$, and we again approximate $\mathrm{v} = \mathrm{v}_\epsilon$. The result of our numerical modeling of P_{e} is summarized in Fig. 8e-f for various Q_{inj}, Q_{ratio} and $y_{\mathrm{separation}}$. For our system, we find $P_{\mathrm{e}} \approx \times 10^2$, that is, $P_{\mathrm{e}} >> 1$, and hence the flow-based confinement dominates over diffusive processes.

4 Temporal Response of the μkiss Brushing

The temporal response of μkiss brushing is defined as the amount of time that is required for the brush envelope to establish itself, following actuation of flow. To characterize the response time, the development of the brush as a function of time is recorded with the envelope extent used to parameterize the envelope, that is, the response time corresponds to the amount of time required for maximum envelope extent to be established. We define the edge of the boundary, to be the point at which the concentration of the envelope falls to 1%.

Figure 9a presents a confocal fluorescence image showing a close-up view of a brush envelope (visualized by inclusion of a fluorescent dye AF488), with the path along which extent is measured. With imaging at a frame time of 44 ms, the intensity of the signal along the path marked 'extent' in Fig. 9a is recorded, and summarized in Fig. 9b for $Q_{\mathrm{inj}} = 0.076\,\mathrm{nL\,s^{-1}}$ and $Q_{\mathrm{asp}} = 3.20\,\mathrm{nL\,s^{-1}}$ for each point in time. The rise-time for the envelope to develop to its maximum extent is, here, 120 ms. Fig. 9(b) and Fig. 9c repeat this measurement for increasingly larger injection flow rates ($Q_{\mathrm{inj}} = 0.687$ and $1.450\,\mathrm{nL\,s^{-1}}$, respectively). The larger brush envelopes that establish, in accordance with the larger injection flow rates, require a slightly longer establishment time, with a rise-time of 168 ms and 220 ms respectively.

5 μkiss & FRAP: Analysis & Modeling

To determine the diffusion constant of AF488-CTxB-labelled GM1 via FRAP microscopy, we follow the analysis procedure outlined in Ref: [3]. For FRAP performed with a confocal bleach spot, the diffusion constant D_{FRAP} can be found via:

$$D_{\mathrm{confocal}} = \frac{r_e^2 + r_n^2}{8\,\tau_{1/2}} \tag{4}$$

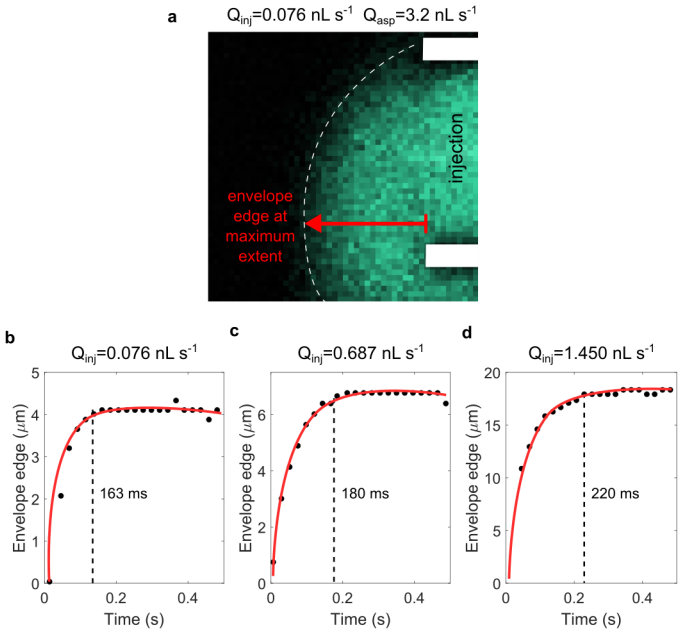

Figure 9: Temporal response of the μkiss envelope a, Confocal fluorescence image of a fluorescently-labelled flow envelope. The dashed line guides the eye to the envelope boundary. The solid red line marks the path along which maximum envelope extent is extracted. The white regions guide the eye to the pipette walls. The envelope extent as a function of time as the envelope is triggered to switch on by flow being initiated, with the rise time is marked for clarity for **b**: $Q_{\mathrm{inj}} = 0.076\,\mathrm{nL\,s^{-1}}$, **c**: $Q_{\mathrm{inj}} = 0.687\,\mathrm{nL\,s^{-1}}$ and **d**: $Q_{\mathrm{inj}} = 1.450\,\mathrm{nL\,s^{-1}}$. In all measurements $Q_{\mathrm{asp}} = 3.20\,\mathrm{nL\,s^{-1}}$.

where r_n is the nominal radius of the bleach spot (from assumed ideal values), r_e is the 'experimental' radius of the bleach spot and is directly measured, and finally $\tau_{1/2}$ is the half-life of the recovering bleached intensity. An example of a FRAP measurement is shown in Fig. 10a. To perform the analysis, on each imaged bleached frame a two-dimensional Gaussian function is fitted to the intensity distribution. From this fit, the peak intensity I of the bleached spot can be extracted, shown in Fig. 10b, for all times during bleaching recovery (yielding $I(t)$). To compute the half-life for bleach recovery, an exponential function of the form $I(t) = a\,e^{(-b\,t)} + c$ is fitted to the extracted amplitudes, where a, b and c are variables to be fitted. The half-life of $I(t)$ is then $\tau_{1/2} = log(2)\,b^{-1}$. The nominal radius of the confocal spot can be calculated via $r_n = \lambda/(4\mathrm{NA})$, where λ is the wavelength (here 488 nm) and NA is the numerical aperture (here, 1.0). The experimental radius can be extracted via the two-dimensional Gaussian function fitted to the first post-bleached frame (such as in Fig. 10a). With these computed, the diffusion D_{FRAP} constant can be calculated.

The framework used to calculate the diffusion constant for a FRAP measurement can also be applied to a μkiss brush labeling measurement, illustrated in Fig. 10(c). To each imaged frame of the CTxB-AF488:GM1 complex, a two-dimensional Gaussian function can be fitted in order to extract the peak amplitude of the labeled spot across time ($I(t)$) - shown in Fig. 10d. Similar to the FRAP analysis, to the $I(t)_{\mu\mathrm{kiss}}$ one can also fit an exponential function to the distribution to yield the half-life of the diffusion-led amplitude decay. As a nominal radius of the spot size is not applicable, we assume $r_n = r_e$, where r_e is extracted from a two-dimensional Gaussian function fitted to the first labeled frame of the set. Following this, the diffusion constant $D_{\mu\mathrm{kiss}}$ can be calculated.

To validate our analysis approach for extracting a diffusion constant from our μkiss measurement, we perform numerical modeling of an analogous system. We use the FRAP modeling framework of Ref:[4], and invert the amplitude so-as to mimic the intensity distribution characteristic of μkiss. Fig. 10e presents a simulated image sequence of diffusion-led broadening of an intensity distribution. We adopt a pixel size similar to that of our imaging confocal microscope pixel size and chose a time resolution of 0.1 s. We assume an initially circular intensity distribution, with radius 1 μm, and with soft edges (convolution with a Gaussian) and add noise to mimic a signal-to-noise ratio (SNR) of 10, as encountered in experiment. Finally, we assert the designed diffusion constant to be $D^{*}_{\mu\mathrm{kiss}} = 0.05\,\mu\mathrm{m}^2\mathrm{s}^{-1}$. Repeating the analysis procedure used for experimental μkiss, outlined above, we compute the model diffusion constant $D^{\mathrm{model}}_{\mu\mathrm{kiss}}$ for $\mathrm{N} = 25$ runs, with a histogram summarizing the distribution in Fig. 10f.

6 Cell Viability Under μkiss Operation

To assess the viability of cells subject to μkiss brush delivery, the LIVE/DEAD assay (Invitrogen, R37601) is used. The LIVE signal indicates metabolic activity and hence cell health, while DEAD signal arises due to a loss of cell membrane integrity and cell death. To firstly verify that we are able to correctly identify both the LIVE and DEAD signals from a sample transitioning from a healthy to distressed state, we perform μkiss brush delivery of an insulting reagent to a select single cell. We chose the insulting reagent to be a 1% Triton X100 membrane detergent solution, which has an immediately lethal effect on the live cell.

Figure 11a presents a dual-channel image of a healthy cell culture labeled with the LIVE/DEAD stain. μkiss brush delivery is performed on the cell marked with the white arrow, additionally depicted in Figure 11b. Post insult, the targeted cell shows a complete absence of the previous LIVE signal, instead displaying a strong DEAD fluorescence signal - shown in Fig. 11c. A time trace of the LIVE and DEAD signal, integrated across the entire cell, for the marked cell is plotted in Fig. 11d wherein the concomitant transition upon insult is observed.

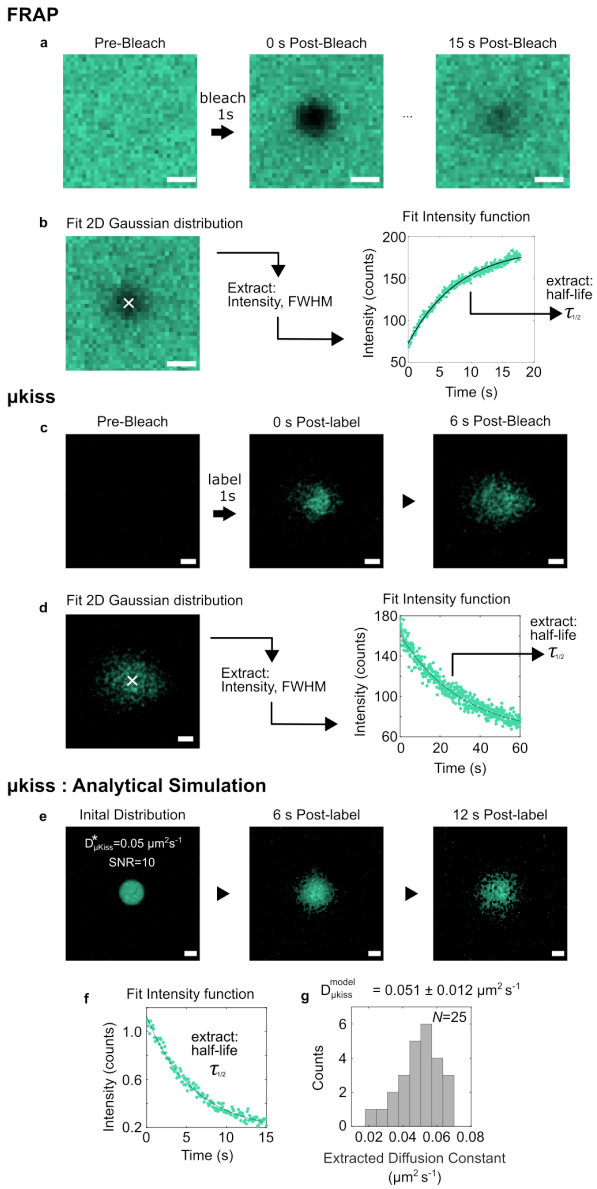

Figure 10: Determination of GM1 diffusion constant for FRAP and μkiss a, Confocal fluorescence image sequence showing FRAP bleach and recovery of the CTxB-AF488:GM1 SLB. **b,** Schematic showing process of parameter extraction from **a**, and characteristic plot of extracted bleached-signal intensity during recovery time from which $\tau_{1/2}$ is fitted. Scale bars in **a** and **b** 1 μm. **b,** Confocal fluorescence image sequence showing μkiss brush labeling and diffusion of CTxB-AF488 labelled GM1 SLB. **d,** Schematic showing process of parameter extraction from **c**, and characteristic plot of extracted signal region over time, from which $\tau_{1/2}$ is fitted. Scale bars in **c** and **d** 1 μm. **e,** Numerical simulation of a μkiss labeling measurement, where mobile species has diffusion constant $D^*_{\mu\text{kiss}}$ and each image frame has a SNR of 10. **f,** Extracted peak signal intensity of the 'labeled' region, following fit of a two-dimensional Gaussian function. **g,** Histogram of extracted diffusion constant of mobile species for $N = 25$ repeated runs.

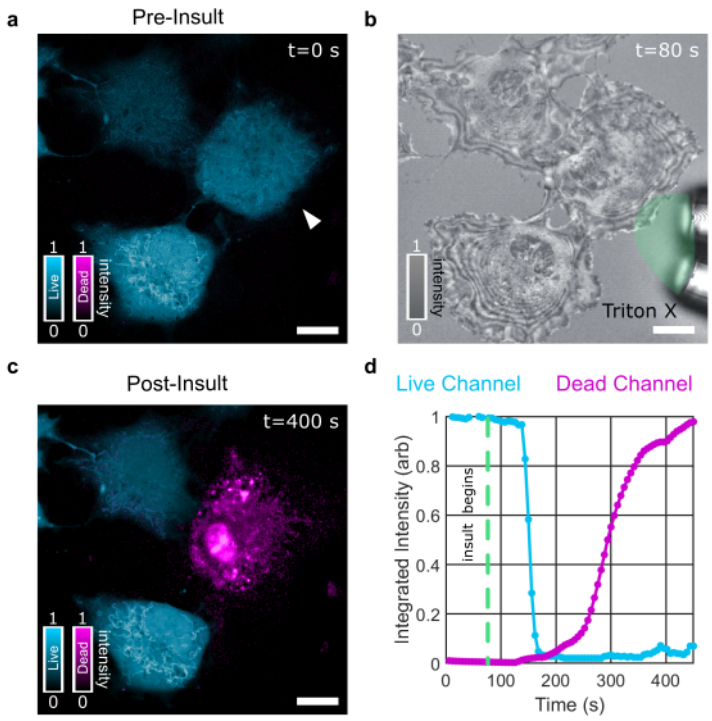

Figure 11: Validating LIVE/DEAD assay on a single cell. **a,** Dual-channel confocal fluorescence image of a cell culture treated with both the LIVE and DEAD label, prior to insult. Arrowhead marks intended target cell. **b,** iSCAT image corresponding to **a**, showing μkiss envelope position and overlay of Triton X100 flow envelope (green). **c,** Dual-channel confocal fluorescence image of the region shown in **a** following Triton X100 delivery to the marked cell of **a**. **d,** Integrated intensity from the marked cell showing the LIVE and DEAD signals as a function of time. Green dashed line denotes start point of Triton X100 insult. Scale bars 5 μm throughout figure.

To now assess the effect of μkiss brush delivery alone on cell health, we perform a similar measurement wherein a benign reagent is applied to the cell, shown in Fig. 12. We chose cell culture medium as the nominal reagent and supplement it with a small quantity of Transferrin-AF647 for visualizing the flow envelope. Fig. 12a presents the target healthy cell which displays an exclusive LIVE signal. Following continuous μkiss brush delivery for 20 minutes, shown in Fig. 12b, inspection reveals an absence of DEAD signal, nor a change in the LIVE signal nor an observable change in the bright-field based iSCAT image. The flow rate here represents the largest used throughout this work ($Q_{\text{inj}} = 0.55\,\text{nL}\,\text{s}^{-1}$ & $Q_{\text{asp}} = 1.60\,\text{nL}\,\text{s}^{-1}$). These results confirm that extended and direct operation of the μkiss brush does not affect viability of the targeted cell.

7 Sub-cellular Delivery Targeting the Microtubule Network

To verify that the observed sub-cellular insult response results from the chemical function of demecolcine, and is not an artefact of the means by which it is delivered, i.e. from μkiss brush delivery, we performed a similar measurement

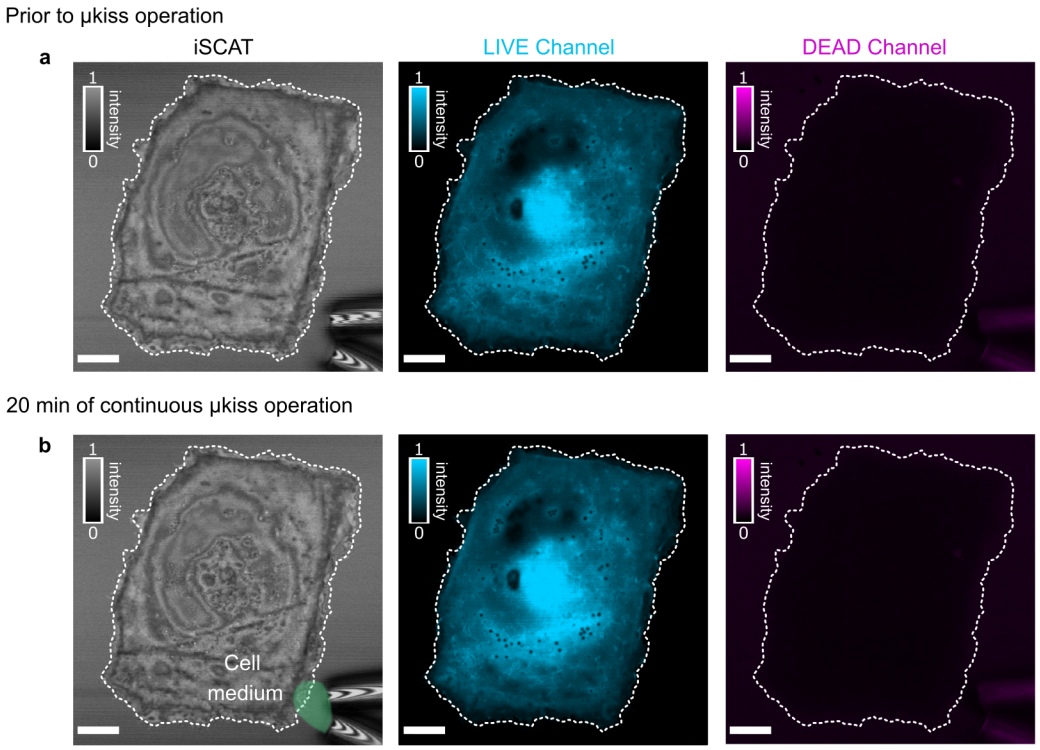

Figure 12: Viability of μkiss brush delivery. **a,** Separate image channels of chosen target cell, prior to μkiss brush operation, viewed as iSCAT (brightfield) as well the LIVE and DEAD fluorescence channels. **b,** Corresponding image channels to **a**, following 20 min of continuous μkiss brushing wherein cell culture medium is locally applied to the region marked by the green overlay. Scale bar is 5 μm throughout.

wherein we deliver warmed Leibovitz's cell culture medium as a benign reagent. Figure 13a shows an iSCAT image of the sub-cellular region of interest, with the outline of the targeting zone marked for reference.

A cell culture is transfected to express GFP throughout the microtubule network, shown in Fig. 13b for the same region. μkiss delivery of warmed Leibovitz's was performed continuously for 10 min at the same experimental conditions of demecolcine application in Fig. 3 ($Q_{\text{inj}} = 0.23\,\text{nL}\,\text{s}^{-1}$ and $Q_{\text{asp}} = 1.59\,\text{nL}\,\text{s}^{-1}$). Confocal fluorescence images following the microtubule network at 5 (Fig. 13c) and 10 min (Fig. 13d) of continuous application reveal an absence of network disruption as it was observed under demecolcine application.

The changes in length of the microtubules affected by demecolcine insult, presented in Fig. 3, is found as follows: Figure 14a presents a confocal fluorescence image of the GFP-labelled microtubule network from Fig. 3, prior to demecolcine insult. Scale bar is 5 μm. Intensity scale used throughout entire figure. The five microtubules under inspection are highlighted in Figure 14, each with a unique color and a star marker denoting the tip location prior to retraction. The result of demecolcine insult leads to retraction of each microtubule, with the retracting tip position marked along the respectively-colored trajectory. The arrow marker indicates the general direction of retraction movement. Each trajectory point corresponds to a subsequent imaging frame of 10 s. Taking the trajectory of tip retraction, a kymograph of GFP-microtubule intensity along this path can be constructed, presented in Fig. 14b for

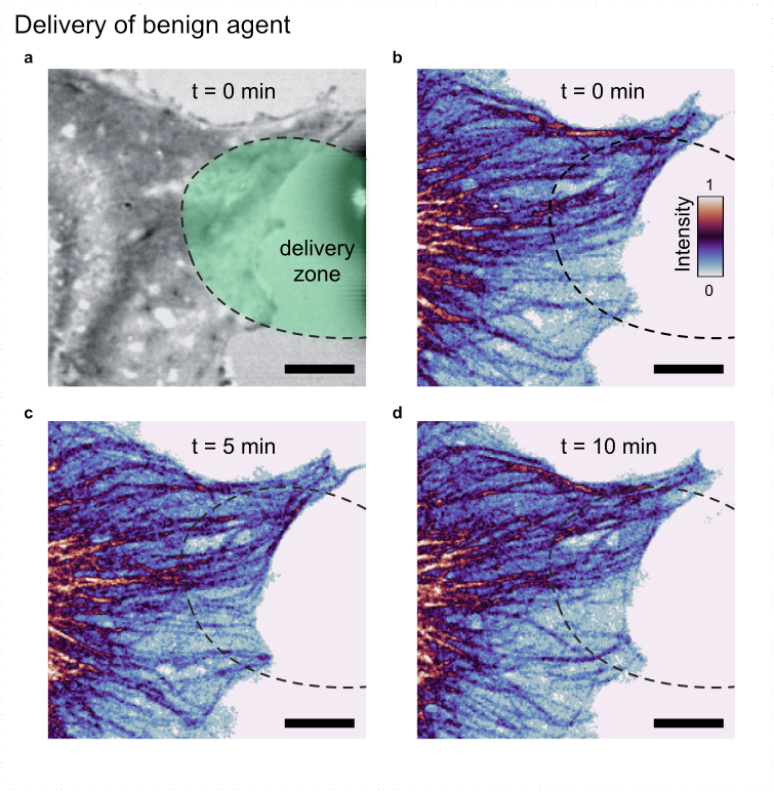

Figure 13: Delivery of a non-insulting reagent does not perturb the microtubuli network. a, iSCAT image of a target cell, to which Leibovitz's medium will be delivered. The region of local delivery is marked in green for reference. **b,** Confocal fluorescence image of the region in **a**, revealing the GFP-labelled microtubule network prior to Leibovitz's delivery. Leibovitz's medium is applied to the marked region continuously and imaged after 5 min, **c**, and 10 min, **d**. Scale bar is 5 μm throughout.

the blue trajectory in Fig. 14a. The star marker denotes again the initial tip position prior to insult. The dashed line in Fig. 14b guides the eye to the tip position during retraction. In Fig. 14c we present the full set of tip retractions along their respective retraction trajectory - written as 'Retraction Length' - as a function of time elapsed since demecolcine application. The length-change here is defined to be negative, to emphasize a net loss in length. One observes the start time of retraction occurs later for microtubules that are initially positioned further away from the μkiss envelope, suggesting indeed a concentration gradient of applied demecolcine within the cell interior.

Upon cessation of demecolcine delivery, 9 min after beginning, shortened microtubules are observed to grow longer and so return to lengths similar to their state prior to demecolcine insult. Figure 14d highlights five such microtubules that undergo a recovery in their length. In analogy to Fig. 14a, the star marker denotes initial tip position prior to recovery. The arrow marks general direction of recovery growth. Each colored data marker plots the tip position for each 10 s imaging frame. A kymograph of the GFP-microtubule intensity along the regrowing trajectory for the tip marked in blue in Fig. 14a is presented in Fig. 14b, with the dashed line guiding the eye to the tip position. The lengths 'regrown' along each recovery trajectory - written as 'Recovery Length' for all five microtubules is plotted in Fig. 14f as a function of time, beginning from the point of demecolcine cessation.

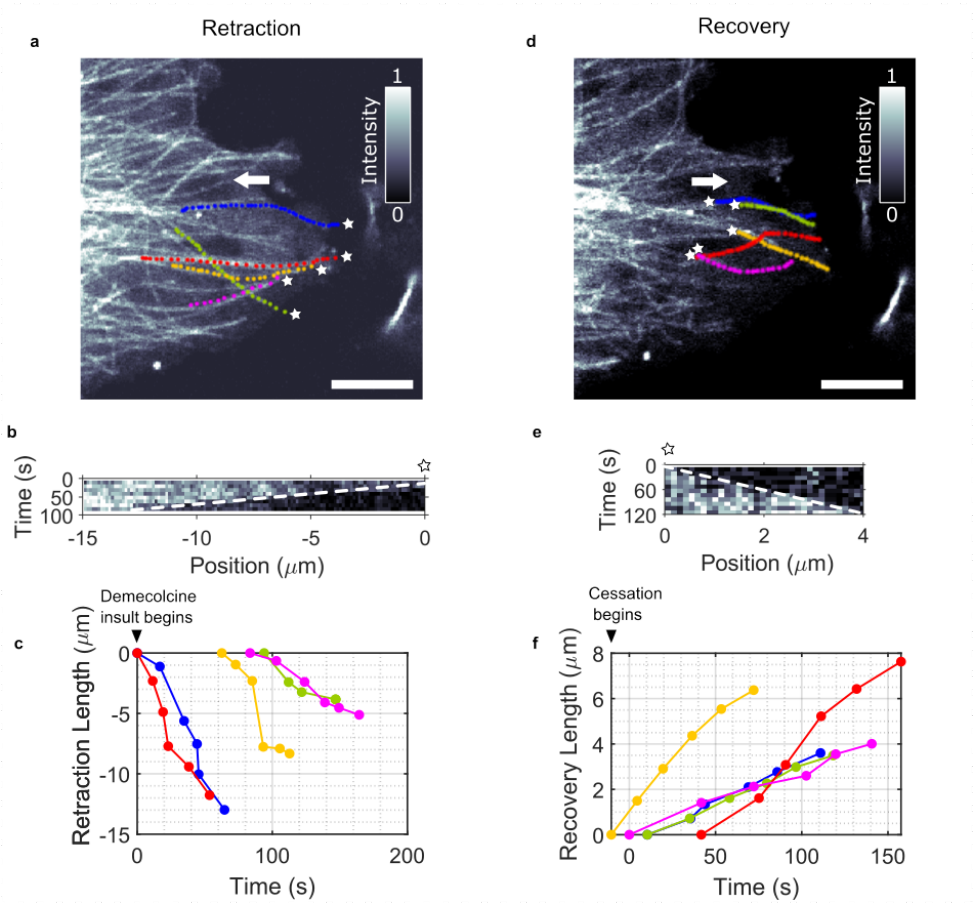

Figure 14: Local-scale retraction and recovery of the microtubule network in response to local demecolcine insult. **a,** Fluorescence image of a cell with the microtubule network labelled with GFP. The positions of the tips from 5 retracting microtubules are plotted as a function of time, with star marker denoting the initial positions. Arrow marker indicates general retraction direction. Scale bar 5 μm. **b,** Kymograph of microtubule retraction for the path labeled blue in **a**. Dashed line guides the eye to the tip position. **c,** The length of microtubule tip retraction for the 5 tips indicated in **a**, as a function of time from point of demecolcine application. **d,** Fluorescence image of the region in **a**, at the point of demecolcine insult cessation. Star markers denotes initial position of microtubule tips, and colored paths respectively indicate the advancing tip positions during regrowth (recovery). Arrow marker denotes direction of regrowth. Scale bar 5 μm. **e,** Kymograph of microtubule recovery for the path labeled blue in **d**. **f,** The length of microtubule tip recovery for the 5 tips indicated in **f**, as a function of time from point of demecolcine insult cessation.

8 Manders' Coefficient of Tf-AF488:Clathrin labeling

In Fig. 4b we present co-labeling of clathrin and TfR, the latter labeled by μkiss brush delivery of Tf-AF647. To quantify the degree of co-localization, we calculate Manders' coefficients m to find the percentage of total signal from one channel which overlaps with signal from the other. Figure 15a presents an iSCAT image of the cell region prior to labeling of Tf-AF647. The clathrin distribution within the marked region post-labeling of Tf-AF647 is shown in Fig. 15b, with the Tf-AF647 signal in the same region shown in Fig. 15c. Dashed line marks the extent of the μkiss brush labeling region. A composite merge of Figs. 15b,c is shown in Fig. 15d for reference.

Following the approach of Supplementary Ref. [5], we compute the coefficients. Here, one channel corresponds to the clathrin signal and the other that of Tf-AF647. We compute the clathrin spatial overlap with Tf-AF647 by summing the intensity of every pixel with clathrin intensity whose corresponding Tf-AF647 pixel is above zero, and normalize to the total original clathrin signal. Doing so we compute $m = 142/295 = 0.62$. Similarly we find for Tf-AF647: $m = 129/183 = 0.71$.

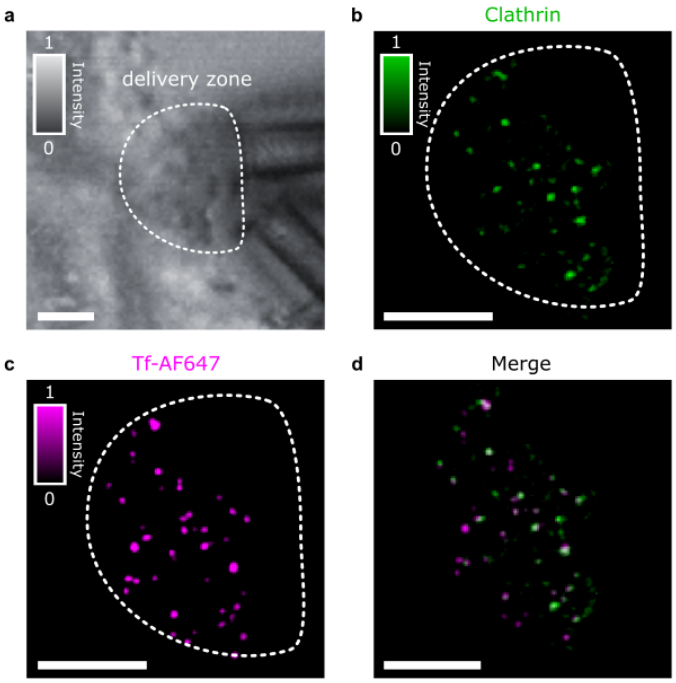

Figure 15: Tf-AF647 & clathrin distribution used for calculating Manders co-localization coefficient. a, iSCAT image of the target cell region, with dashed line marking the labeling area. **b,** Fluorescence image showing clathrin distribution within the dashed region from **a** at the point immediately following Tf-AF647 delivery to the dashed region. **c,** Fluorescence image showing Tf-AF647 distribution on the membrane immediately following Tf-AF647 delivery. **d,** Merged image of the channels from **b** and **c**, showing their spatial overlap. Scale bar is 5 μm throughout.

9 Quantifying TfR labeling

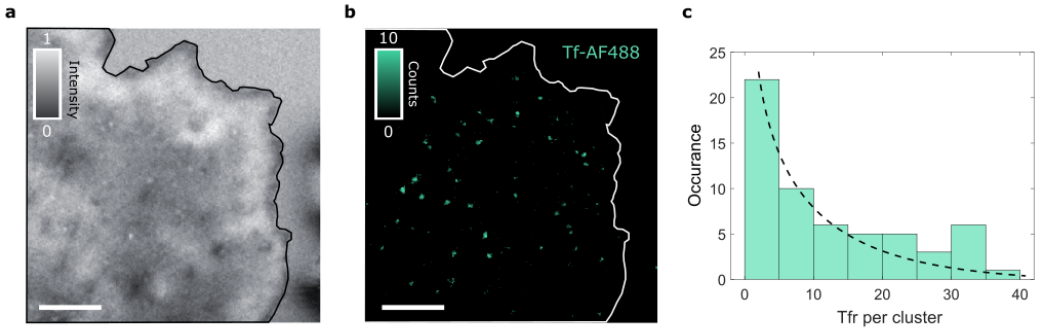

Figure 16: Quantification of the number of TfR labelled within each membrane cluster. a, Confocal iSCAT image of the cell region to which μkiss brush labeling of TfR with Tf-AF488 will occur. Black line marks cell boundary for reference. **b,** Fluorescence image from the same membrane region as **a**, following Tf-AF488 delivery and labeling of TfR clusters. Scale bars in **a** and **b** are 5 μm. **c,** Histogram showing the calibrated number of TfR per cluster from the image in **b**.

To estimate the number of TfR that we label with μkiss brush delivery of Tf-AF488, we need to calibrate the optical signal of Tf-AF488 to the number of Tf present, assuming 1:1 binding of Tf and TfR. To begin, we first quantify the ratio of AF488 to Tf in our labeling reagent solution. We use a NanoPhotometer (Implen GmbH) to measure the optical extinction of our 2 mg ml^{-1} Tf-AF488 solution, and find the concentration of AF488 to be four-fold higher than that of the Tf, giving a labeling ratio of 4:1. At a working Tf-AF488 concentration of 2 mg ml^{-1}, Tf is present as $C_{\mathrm{Tf}} = 15055$ molecules μm^{-3} and AF488 as $C_{\mathrm{AF488}} = 60220$ molecules μm^{-3}.

Next, we consider the properties of our imaging confocal microscope. The volume of the confocal PSF is computed via:

$$V_{\mathrm{PSF}} = \frac{2.33\,\pi^{3/2} n\, w^3}{\mathrm{NA}} \tag{5}$$

where $n = 1.33$ is the refractive index of the medium (water), the numerical aperture NA = 1.0 and w is the e^{-2} beam radius in the xy-plane. We assume a wavelength of 510 nm (peak fluorescence emission of AF488 detected here), and find $V_{\mathrm{PSF}} = 0.561\ \mu$m^{-3}. We establish a μkiss envelope with concentration $C_{\mathrm{AF488}} = 60220$ molecules μm^{-3} and record the signal intensity with the same acquisition settings as used in the original labeling measurement. We find from within the confocal PSF detection volume a median signal intensity of $I_{\mathrm{det}} = 117$ counts s^{-1} from AF488. This signal is assumed to originate from $V_{\mathrm{PSF}} \times C_{\mathrm{AF488}}$ molecules, that is, $N_{\mathrm{AF488}} = 33790$ molecules. This equates to an average of 3.45×10^{-3} counts s^{-1} per AF488, which is equivalently 0.0138 counts s^{-1} per Tf.

In Fig. 16a we present a confocal iSCAT image of the cell membrane region[6,7], that undergoes Tf-AF488 μkiss brush delivery, yielding AF488-Tf labeled TfR clusters shown in Fig. 16b. Using our calibration, we convert the measured optical signal for AF488 in Fig. 16b, assuming that each distinct cluster is well approximated as originating from a single PSF detection volume. In Fig. 16c we plot the distribution of the calculated number of TfR-per-cluster from Fig. 16b using our signal-to-molecule number calibration.

10 Latrunculin Insult

Lat-A application to the targeted cell in Fig. 5 results in the inward retraction of the cell corpus, shown in Supplementary Video 5. This is manifested in the reduction of the surface area the cell occupies on the substrate. In Fig. 17, we visualize the changing substrate area occupied by the cell that results from application of Lat-A over the full course of the measurement depicted in Fig. 5.

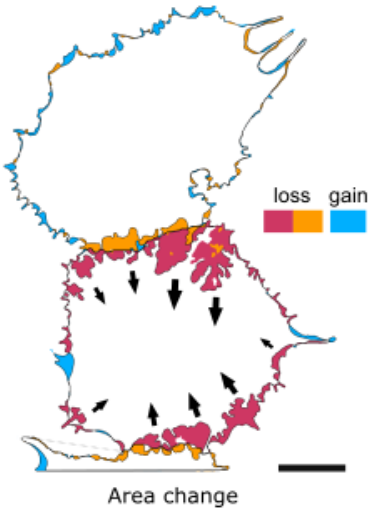

Figure 17: Change in surface area occupied by the targeted and neighboring cells, following Lat-A delivery. White denotes an unchanged area covered by the cells prior to, and following Lat-A delivery. Red and orange denote regions where cell area is lost following Lat-A delivery for the targeted and neighboring cells, respectively. Different colors are used for clarity. Blue regions denote any gain in area covered following Lat-A delivery.

References

[1] Richard W. Taylor, Reza Gholami Mahmoodabadi, Verena Rauschenberger, Andreas Giessl, Alexandra Schambony, and Vahid Sandoghdar. Interferometric scattering microscopy reveals microsecond nanoscopic protein motion on a live cell membrane. *Nat. Photon.*, 13:480–487, 2019.

[2] Anna D Kashkanova, Martin Blessing, André Gemeinhardt, Didier Soulat, and Vahid Sandoghdar. Precision size and refractive index analysis of weakly scattering nanoparticles in polydispersions. *Nat. Meth.*, 19:586–593, 2022.

[3] Minchul Kang, Charles A. Day, Anne K. Kenworthy, and Emmanuele DiBenedetto. Simplified equation to extract diffusion coefficients from confocal frap data. *Traffic*, 13:1589–1600, 2012.

[4] Magnus Röding, Leander Lacroix, Annika Krona, Tobias Gebäck, and Niklas Lorén. A highly accurate pixel-based frap model based on spectral-domain numerical methods. *Biophys. J.*, 116:1348–1361, 2019.

[5] E.M.M. Manders, F.J. Verbeek, and J.A. Aten. Measurement of co-localization of objects in dual-colour confocal images. *J. Microsc.*, 169:375–382, 1993.

[6] Yi-Teng Hsiao, Tsai-Ying Wu, Bo-Kuan Wu, Shi-Wei Chu, and Chia-Lung Hsieh. Spinning disk interferometric scattering confocal microscopy captures millisecond timescale dynamics of living cells. *Opt. Expr.*, 30:45233–45245, 2022.

[7] Michelle Küppers, David Albrecht, Anna D. Kashkanova, Jennifer Lühr, and Vahid Sandoghdar. Confocal interferometric scattering microscopy reveals 3D nanoscopic structure and dynamics in live cells. *Nat. Commun.*, 14:1962, 2023.